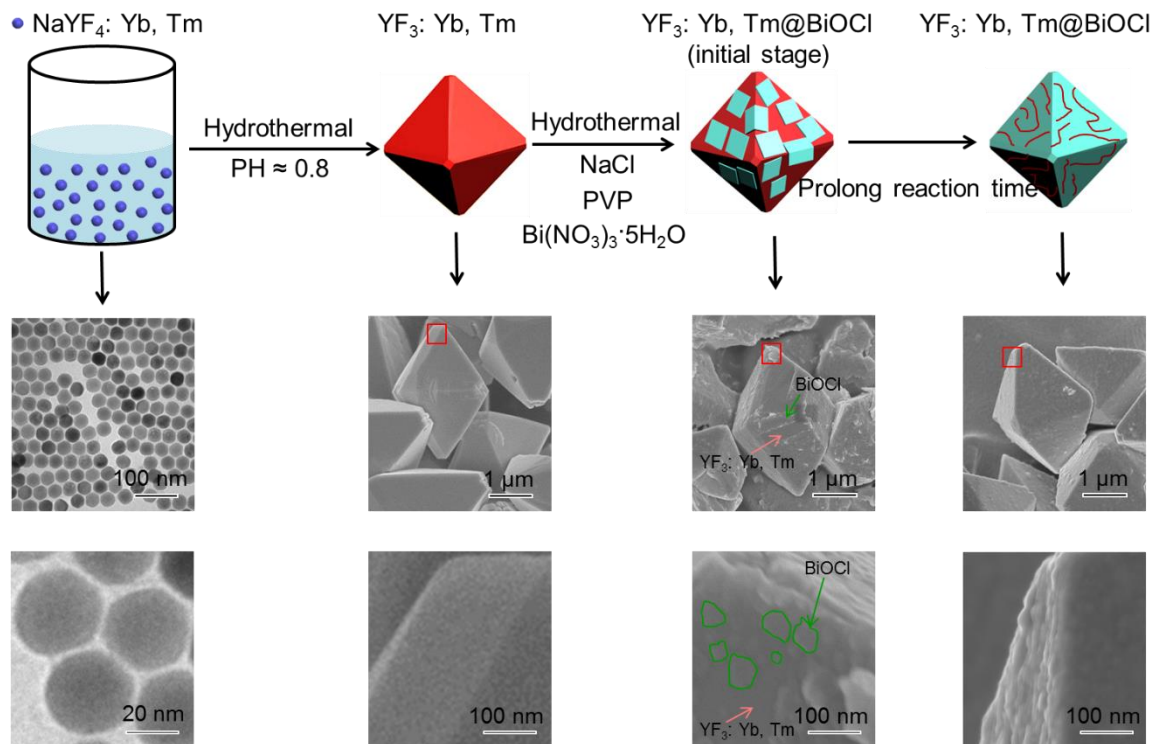


## Supporting Information

### **Boosting NIR-driven photocatalytic water splitting by constructing 2D/3D epitaxial heterostructures**

Li Wang,<sup>a,g</sup> Dandan Cui,<sup>b,c</sup> Long Ren,<sup>a</sup> Jiajia Zhou,<sup>d</sup> Fan Wang,<sup>d</sup> Gilberto Casillas,<sup>e</sup> Xun Xu,<sup>a,c</sup> Germanas Peleckis,<sup>a</sup>  
Weichang Hao,<sup>b,c\*</sup> Jinhua Ye,<sup>f</sup> Shi Xue Dou,<sup>a</sup> Dayong Jin,<sup>d\*</sup> Yi Du<sup>a,c\*</sup>



**Figure S1.** Schematic illustration of the synthesis of  $\text{YF}_3: \text{Yb, Tm}@ \text{BiOCl}$ . TEM images of the original  $\text{NaYF}_4: \text{Yb, Tm}$  with SEM images of the particles at each step also presented.

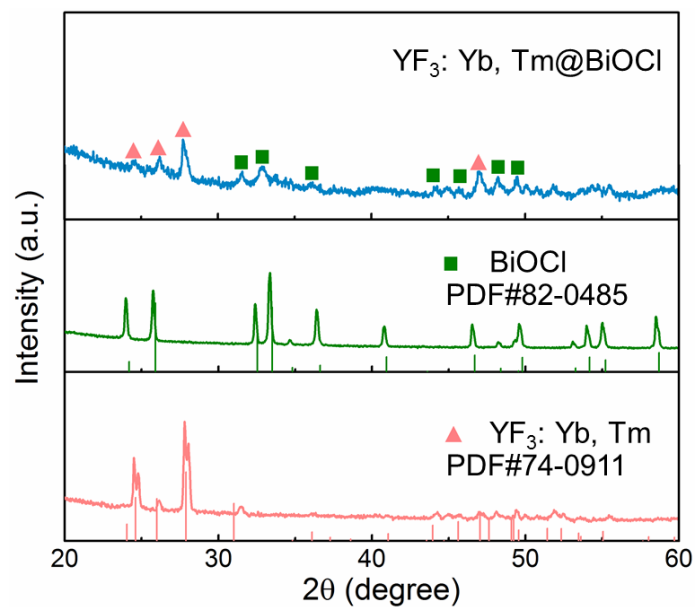


**Figure S2.** XRD patterns of the as-prepared  $\text{YF}_3: \text{Yb, Tm}@ \text{BiOCl}$ ,  $\text{YF}_3: \text{Yb, Tm}$ , and  $\text{BiOCl}$ . The standard patterns from the PDF cards for  $\text{BiOCl}$  and  $\text{YF}_3: \text{Yb, Tm}$  are also presented. The X-ray diffraction peaks of  $\text{YF}_3: \text{Yb, Tm}@ \text{BiOCl}$  can be indexed to the orthorhombic  $\text{YF}_3: \text{Yb, Tm}$ .

Tm and the tetragonal BiOCl, indicating that the YF<sub>3</sub>: Yb, Tm@BiOCl core-shell structure consists of YF<sub>3</sub>: Yb, Tm and BiOCl.

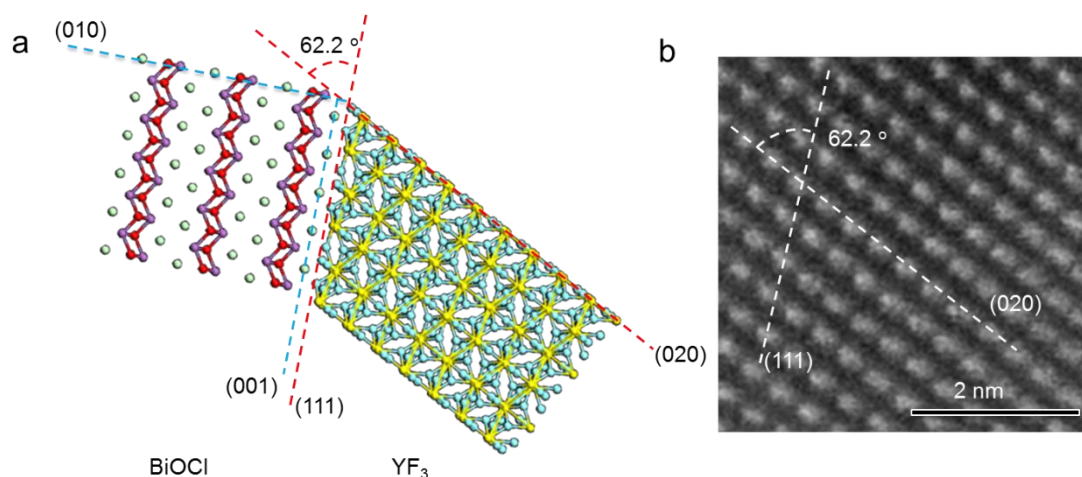


**Figure S3. a**, Theoretical modelling of BiOCl epitaxial growth on YF<sub>3</sub>. The lattice spacing of (010) planes of BiOCl is 0.389 nm, and the lattice spacing of the (020) plane at the interface with the (111) planes of YF<sub>3</sub> is 0.384 nm. The mismatch between the (010) plane and the (020) plane is around 0.6%, which provides the possibility of epitaxial growth in view of the structural compatibility. **b**, High-resolution TEM image of YF<sub>3</sub> with the indexed planes labelled. The colours of the atoms are: Cl: light green, Bi: purple, O: red, F: yellow, Y: light blue. Combining (a) and (b), it is obvious that the (001) plane of BiOCl is epitaxially grown on the (111) plane of YF<sub>3</sub>.

As is well documented, the theoretical values of angles for two different (h, k, l) planes can be evaluated by the following equation:<sup>1</sup>

$$\cos \varphi = \frac{\frac{h_1 h_2}{a^2} + \frac{k_1 k_2}{b^2} + \frac{l_1 l_2}{c^2}}{\sqrt{\left(\frac{h_1^2}{a^2} + \frac{k_1^2}{b^2} + \frac{l_1^2}{c^2}\right) \left(\frac{h_2^2}{a^2} + \frac{k_2^2}{b^2} + \frac{l_2^2}{c^2}\right)}}$$

in which,  $h$ ,  $k$ , and  $l$  are the Miller indices of the plane, and  $a$ ,  $b$ , and  $c$  are the lattice constants. Thus, the angle between the (111) and (020) planes of YF<sub>3</sub> can be estimated to be 62.2°, which is consistent with the observed values in the high-resolution TEM image in Figure S3b. The consistency between the theoretical value and the experimental one for the interfacial angle

between the (111) and (020) planes indicates that the exposed facet of  $\text{YF}_3$  is the {111} facet, on which the {001} highly active facet of  $\text{BiOCl}$  was epitaxially grown, as presented in Figure S3a.

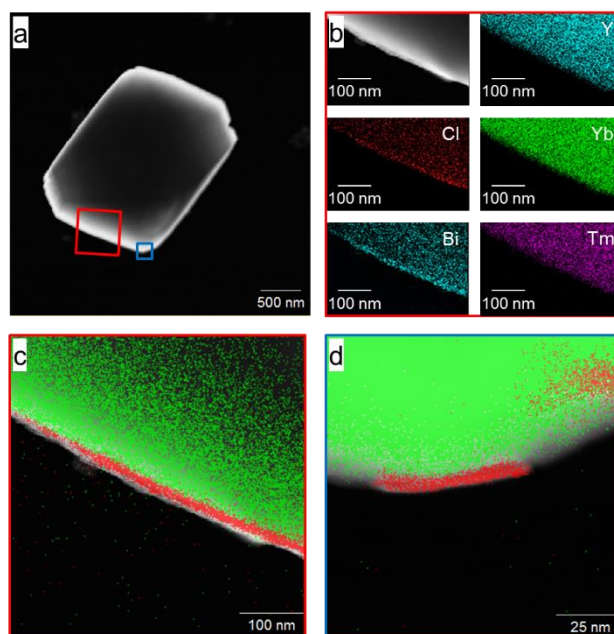


**Figure S4.** **a**, HAADF-STEM image of  $\text{YF}_3$ : Yb, Tm@ $\text{BiOCl}$ . **b**, Typical TEM image and the corresponding elemental mappings for the selected area in **a**. **c**, **d**, Phase mappings of  $\text{YF}_3$ : Yb, Tm@ $\text{BiOCl}$  for the selected area in **a**. As is illustrated, the microparticle includes two phases, the bulk phase and the outer-layer phase. From the elemental mapping results for Bi, Cl, Y, Yb, and Tm in Figure S4b, it can be concluded that the bulk phase is  $\text{YF}_3$ : Yb, Tm, while the outer-layer phase is  $\text{BiOCl}$ . In addition, it is worth noting that the curvature of the  $\text{BiOCl}$  phase at the corner of the microparticle is close to that of the  $\text{YF}_3$ : Yb, Tm phase, revealing that the  $\text{BiOCl}$  is coated on the surface of  $\text{YF}_3$ : Yb, Tm through chemical bonding instead of physical adsorption.

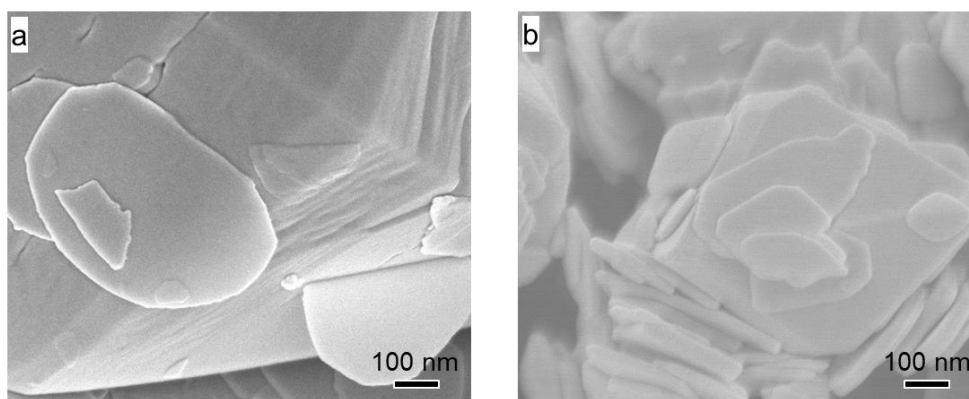


**Figure S5.** **a**, SEM image of YF<sub>3</sub>: Yb, Tm@BiOBr. **b**, SEM image of YF<sub>3</sub>: Yb, Tm@BiOCl nanoplate.

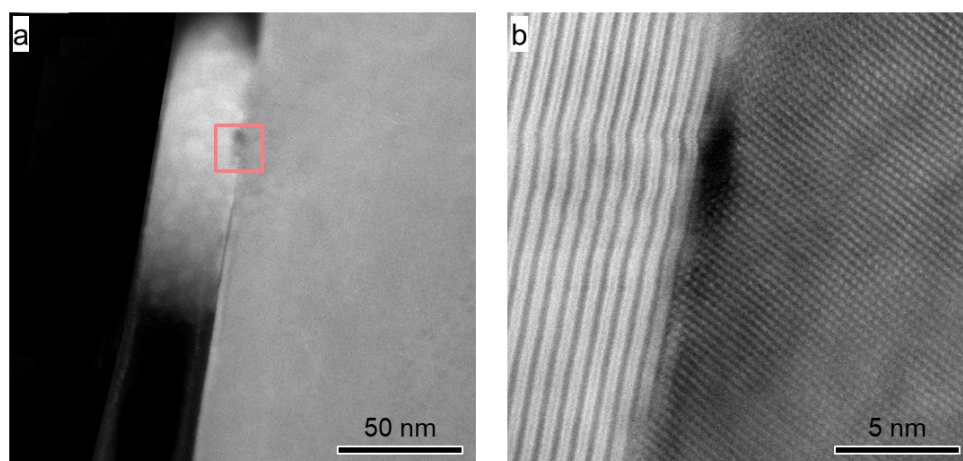


**Figure S6.** **a**, HAADF-STEM image of FIB-milled YF<sub>3</sub>: Yb, Tm@BiOCl nanoplate heterostructure. **b**, High-resolution TEM image of YF<sub>3</sub>: Yb, Tm@BiOCl nanoplate heterostructure for the selected area marked red in (a).

In order to check whether the strategy to construct epitaxial heterogeneous structure for YF<sub>3</sub>: Yb, Tm and ultrathin-nanosheet BiOCl can be applied to other 2D materials, we prepared YF<sub>3</sub>: Yb, Tm@BiOCl and YF<sub>3</sub>: Yb, Tm@BiOBr in which BiOCl and BiOBr are nanoplate-like 2D materials with the surface dimension in micro level. It is obvious that the 2D material with flat surface becomes bending when it is attached to the ridge of the octahedral YF<sub>3</sub>: Yb, Tm, indicating that the 2D material is attached to the surface of YF<sub>3</sub>: Yb, Tm by chemical interaction. These results provide a way for the design of other 2D-3D epitaxial heterogeneous structure.

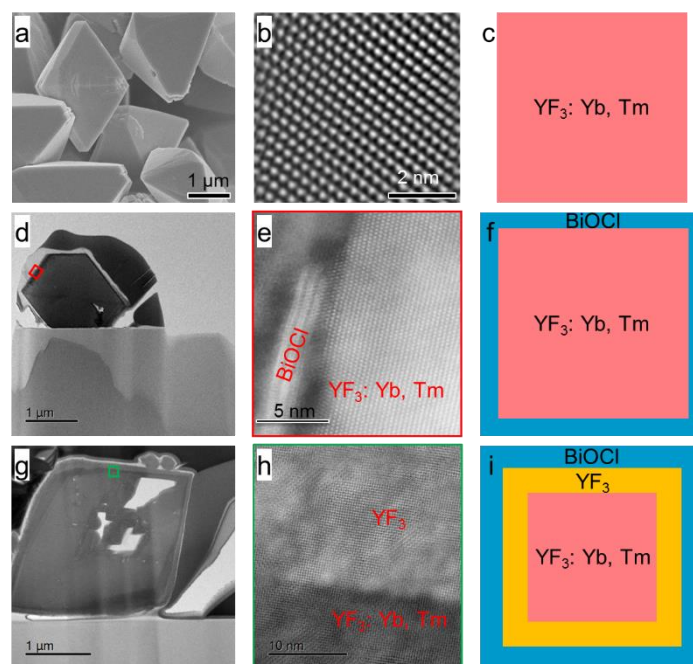


**Figure S7.** **a**, SEM image of YF<sub>3</sub>: Yb, Tm. **d**, **g**, HAADF-STEM images of FIB-milled YF<sub>3</sub>: Yb, Tm@BiOCl particle (**d**) and YF<sub>3</sub>: Yb, Tm@YF<sub>3</sub>@BiOCl (**g**). **b**, **e**, **h**, High-resolution TEM images of the selected areas in **a**, **d**, and **g**, respectively. **c**, **f**, **i**, Schematic illustrations of the structures in **a**, **d**, and **g**, respectively.

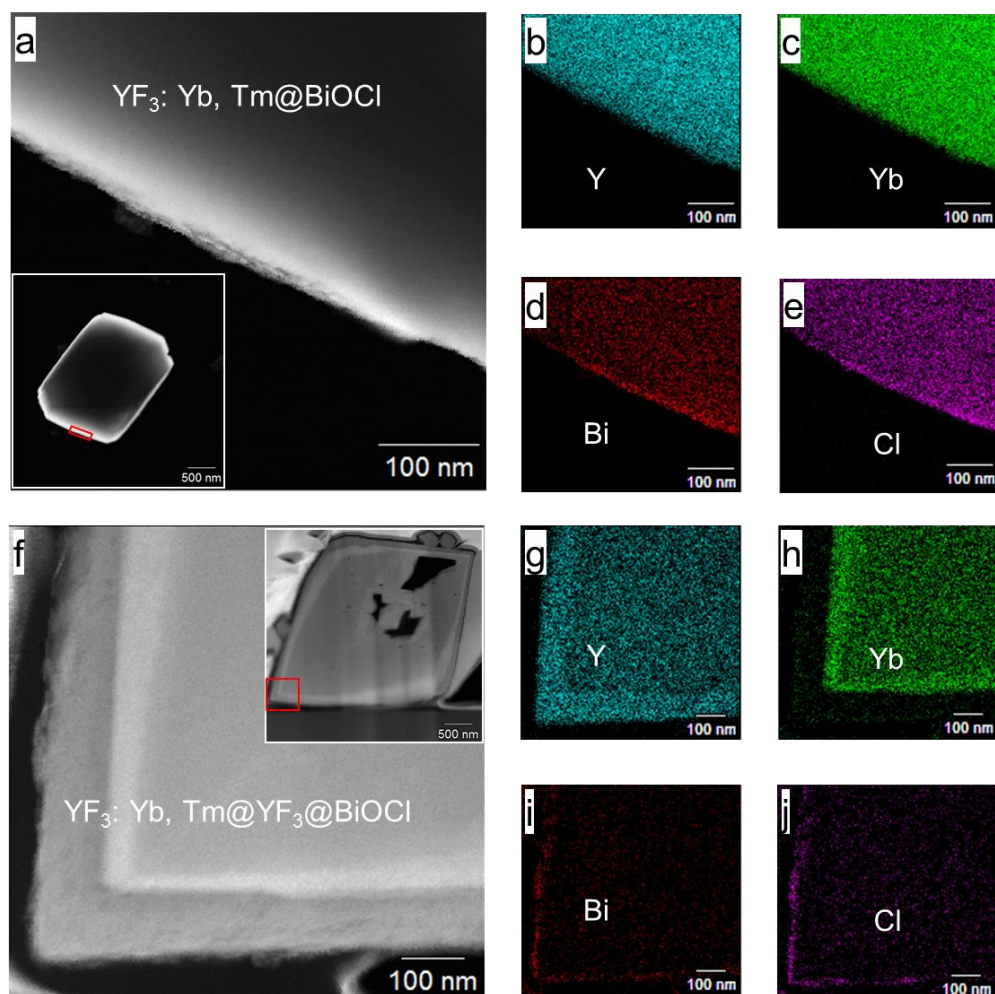


**Figure S8.** **a, f**, Typical TEM images of selected areas in the corresponding inset images for  $\text{YF}_3: \text{Yb, Tm@BiOCl}$  particle (**a**) and  $\text{YF}_3: \text{Yb, Tm@YF}_3\text{@BiOCl}$  particle (**f**). **b-e**, Elemental mappings of Y, Yb, Bi, and Cl for the area of  $\text{YF}_3: \text{Yb, Tm@BiOCl}$  in **a**. **g-j**, Elemental mappings of Y, Yb, Bi and Cl for  $\text{YF}_3: \text{Yb, Tm@YF}_3\text{@BiOCl}$  in **f**.

Apart from the excited state energy transfer (energy transfer), fluorescence reabsorption (photon transfer) is also proposed to occur at the interface region between  $\text{YF}_3: \text{Yb, Tm}$  and  $\text{BiOCl}$ . As the Förster resonance energy transfer and Dexter electron transfer are sensitive to the distance between the donor and acceptor, coating an additional blocking layer with enough thickness between  $\text{YF}_3: \text{Yb, Tm}$  and  $\text{BiOCl}$  is necessary to study the participation of photon transfer in the photocatalytic process.  $\text{YF}_3$  without lanthanide ion doping is an ideal candidate material for the blocking layer, as it cannot absorb the photons upconverted by  $\text{YF}_3: \text{Yb, Tm}$  and cannot provide the intermediate energy levels for the energy migration.<sup>2</sup> In this way, the

photon energy transfer between YF<sub>3</sub>: Yb, Tm and BiOCl will not be influenced, and the excited state energy transfer forms are efficiently blocked after suitable thickness of YF<sub>3</sub> has been introduced.

STEM was used to confirm the structure of YF<sub>3</sub>: Yb, Tm@YF<sub>3</sub>@BiOCl. Figure S7 demonstrates the morphologies and crystal structures of YF<sub>3</sub>, Yb, Tm, YF<sub>3</sub>: Yb, Tm@BiOCl, and YF<sub>3</sub>: Yb, Tm@YF<sub>3</sub>@BiOCl with the schematic illustrations of structures displayed in Figure S7e, f, and i. The sharp contrast in the Figure S7g-h reveals that the blocking layer of YF<sub>3</sub> was successfully introduced into YF<sub>3</sub>: Yb, Tm@BiOCl, which was further confirmed by the EDS elemental mapping of Y, Yb, Bi, and Cl for YF<sub>3</sub>: Yb, Tm@BiOCl and YF<sub>3</sub>: Yb, Tm@YF<sub>3</sub>@BiOCl particles shown in Figure S8.

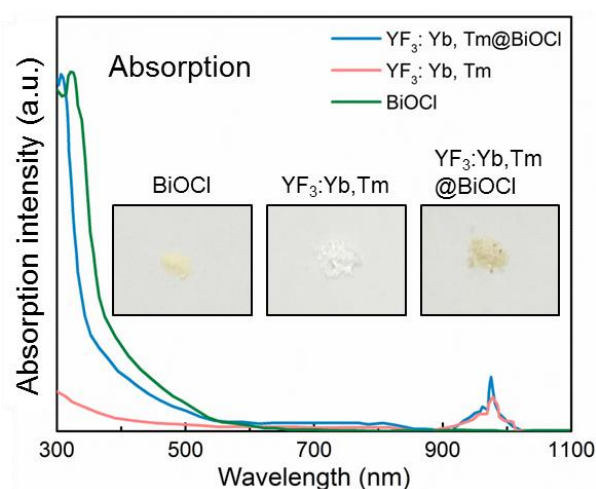


**Figure S9.** UV-visible diffuse reflectance spectra of YF<sub>3</sub>: Yb, Tm, BiOCl and YF<sub>3</sub>: Yb, Tm@BiOCl.

As shown in Figure S9, light absorption of the YF<sub>3</sub>: Yb, Tm@BiOCl particles was characterized by the ultraviolet-visible (UV-vis) diffuse reflectance spectroscopy. Pure YF<sub>3</sub>: Yb, Tm microparticles and ultrathin BiOCl nanosheets were also selected as reference samples. YF<sub>3</sub>: Yb, Tm microparticles possess absorption bands in the UV region, and a featured NIR absorption peak centred at about 980 nm arising from the  $^2F_{7/2} \rightarrow ^2F_{5/2}$  transition of Yb<sup>3+</sup> ions.<sup>3</sup> The ultrathin BiOCl nanosheets show a strong UV absorption with clear absorption edge at about 400 nm and an absorption tail extended to 700 nm in the visible light region. The

absorption edge and tail correspond to the band gap ( $E_g = 3.0$  eV) and surface defect states,<sup>4</sup> respectively. For  $\text{YF}_3$ : Yb, Tm@BiOCl particles, the absorption spectrum shows the absorption characteristics of both BiOCl and  $\text{YF}_3$ : Yb, Tm. Interestingly, the NIR absorption of  $\text{YF}_3$ : Yb, Tm was not suppressed after the epitaxial growth of BiOCl, indicating the epitaxial alignment does not influence the absorption of  $\text{YF}_3$ : Yb, Tm and the photon scattering is not presented at the epitaxial interface.

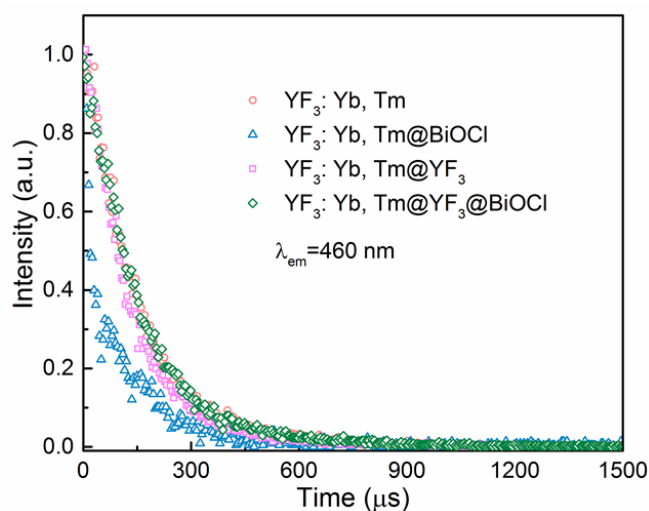


**Figure S10.** Decay curves of single  $\text{YF}_3$ : Yb, Tm,  $\text{YF}_3$ : Yb, Tm@BiOCl,  $\text{YF}_3$ : Yb, Tm@ $\text{YF}_3$  and  $\text{YF}_3$ : Yb, Tm@ $\text{YF}_3$ @BiOCl at 460 nm ( $\text{Tm}^{3+}$ :  $^1\text{G}_4 \rightarrow ^3\text{H}_6$ ) with the excitation of 980 nm laser.

The corresponding  $\text{Tm}^{3+}$ :  $^1\text{G}_4 \rightarrow ^3\text{H}_6$  transition with lifetimes decreasing from 143  $\mu\text{s}$  to 45  $\mu\text{s}$  after the epitaxial growth of BiOCl (Figure 3h), clearly proves the ET pathway from  $\text{Tm}^{3+}$   $^1\text{D}_2$  excited state to the CB of BiOCl.

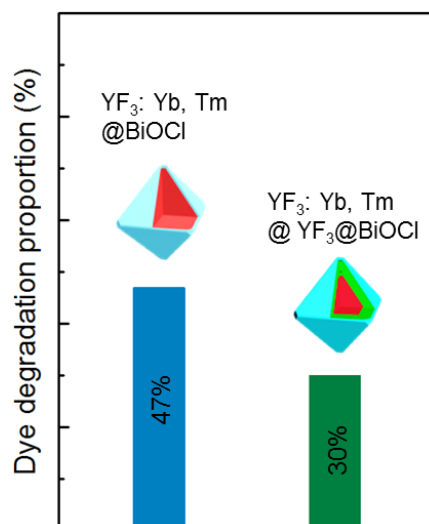


**Figure S11.** Dye degradation proportions of YF<sub>3</sub>: Yb, Tm@BiOCl and YF<sub>3</sub>: Yb, Tm@YF<sub>3</sub>@BiOCl.

RhB photocatalytic degradation under illumination with a wavelength longer than 780 nm was carried out to investigate whether photon transfer occurs in YF<sub>3</sub>: Yb, Tm@BiOCl. It can be observed in Figure S11 that the degradation rate of RhB in the presence of YF<sub>3</sub>: Yb, Tm@YF<sub>3</sub>@BiOCl reaches 30% after 2 h when driven by NIR light, which is less than 47% for YF<sub>3</sub>: Yb, Tm@BiOCl over the same period. The degradation rate of Yb, Tm@YF<sub>3</sub>@BiOCl is about 63% of that of Yb, Tm@BiOCl. As the introduction of YF<sub>3</sub> cannot influence the phonon energy transfer between YF<sub>3</sub>: Yb, Tm and BiOCl, the decrease in the RhB degradation of about 37% for YF<sub>3</sub>: Yb, Tm@YF<sub>3</sub>@BiOCl can be mainly ascribed to the blocking of direct forms of energy transfer by YF<sub>3</sub>, indicating that the photon transfer forms truly contribute to the photocatalytic process in YF<sub>3</sub>: Yb, Tm@BiOCl.

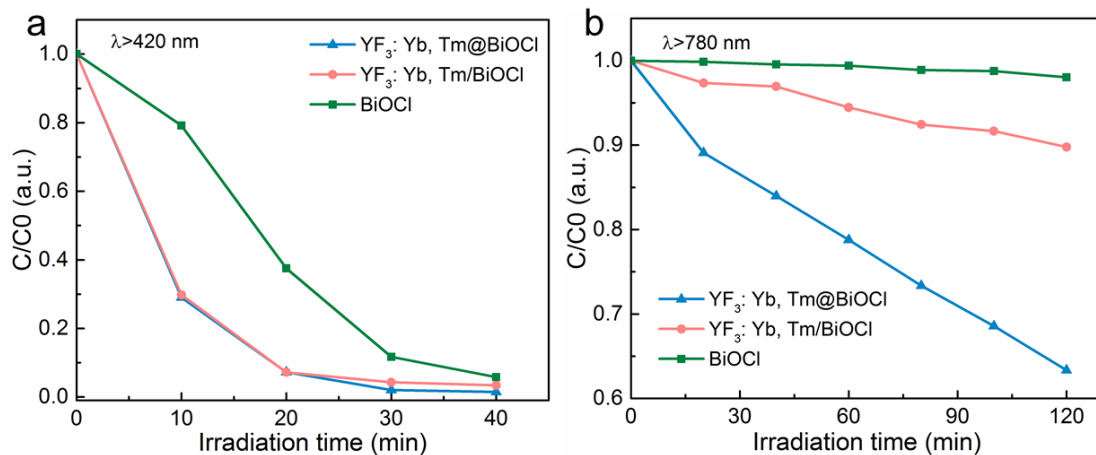


**Figure S12. a, b,** Variation of RhB concentrations as a function of illumination time for YF<sub>3</sub>: Yb, Tm@BiOCl, and a mechanical mixture of YF<sub>3</sub>: Yb, Tm/BiOCl and pure BiOCl nanosheets under illumination by light with wavelength longer than 420 nm (**a**) and NIR light ( $\lambda > 780$  nm) (**b**). The ratio of photocatalyst to dye aqueous solution used in **a** is 3 mg/9 ml. The ratio of photocatalyst to dye aqueous solution used in **b** is 3 mg/3 ml.

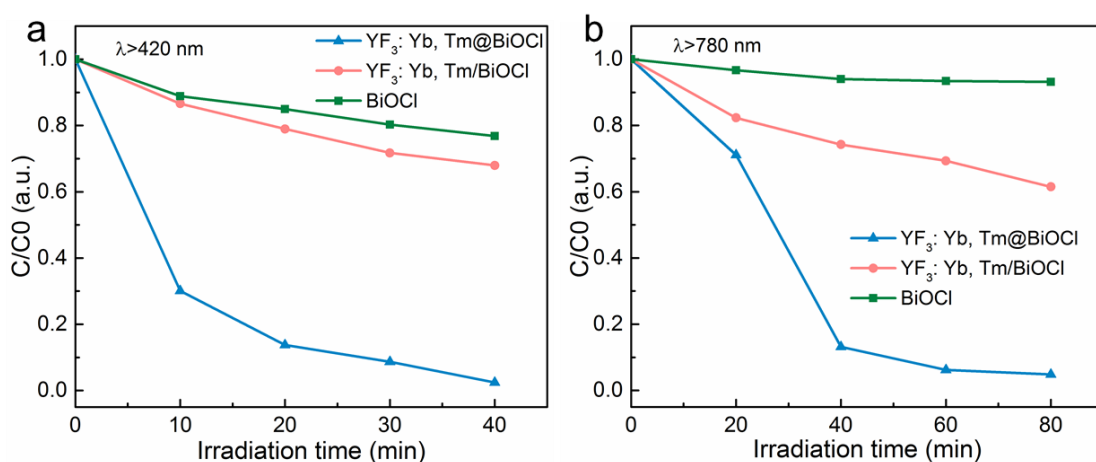


**Figure S13. a,b,** Variation of MB concentrations as a function of illumination time for YF<sub>3</sub>: Yb, Tm@BiOCl, a mechanical mixture of YF<sub>3</sub>: Yb, Tm/BiOCl, and pure BiOCl nanosheets under illuminations by light with wavelengths longer than 420 nm (**a**) and NIR light ( $\lambda > 780$  nm) (**b**). The ratio of photocatalyst to dye aqueous solution used in **a** is 3 mg/6 ml. The ratio of photocatalyst to dye aqueous solution used in **b** is 3 mg/3 ml.

RhB and MB were selected as the probe molecules to test whether YF<sub>3</sub>: Yb, Tm@BiOCl can show photocatalytic activity towards various species of pollutants. As depicted in Figure S12a,

the RhB degradation by YF<sub>3</sub>: Yb, Tm@BiOCl and the mechanical mixture of YF<sub>3</sub>: Yb, Tm/BiOCl under irradiation by light with wavelengths longer than 420 nm is close to 100% in 30 min in both cases, while nearly 88% of RhB molecules were degraded by pure BiOCl in the same period. Compared with RhB, the difference in the degradation performance of MB for the three tested samples is more obvious. Figure S12a demonstrates that under irradiation by light with wavelengths longer than 420 nm, the degradation rate of MB in the presence of YF<sub>3</sub>: Yb, Tm@BiOCl reaches 100% in 80 min, while only 40% of MB molecules were degraded by YF<sub>3</sub>: Yb, Tm/BiOCl and only 20% of MB molecules were degraded by BiOCl over the same period. The observed difference in the RhB and MB degradation performances can be ascribed to the different charge types on the surfaces of these two dyes. The NIR-light-driven ( $\lambda > 780$  nm) RhB degradation rate of YF<sub>3</sub>: Yb, Tm@BiOCl is 2.5 times higher than for YF<sub>3</sub>: Yb, Tm/BiOCl as shown in Figure S12b, and the NIR-light-driven MB degradation of YF<sub>3</sub>: Yb, Tm@BiOCl is 2.5 times as great as for YF<sub>3</sub>: Yb, Tm/BiOCl, as displayed in Figure S13b. In contrast, no obvious degradation of RhB molecules and MB molecules was observed in the presence of pure BiOCl nanosheets under the NIR illumination ( $\lambda > 780$  nm), which is because BiOCl cannot absorb the NIR light. The superior RhB and MB degradation over the whole wavelength range suggests that the introduction of YF<sub>3</sub>: Yb, Tm upconversion particles can help to broaden the utilization of solar energy by YF<sub>3</sub>: Yb, Tm@BiOCl.

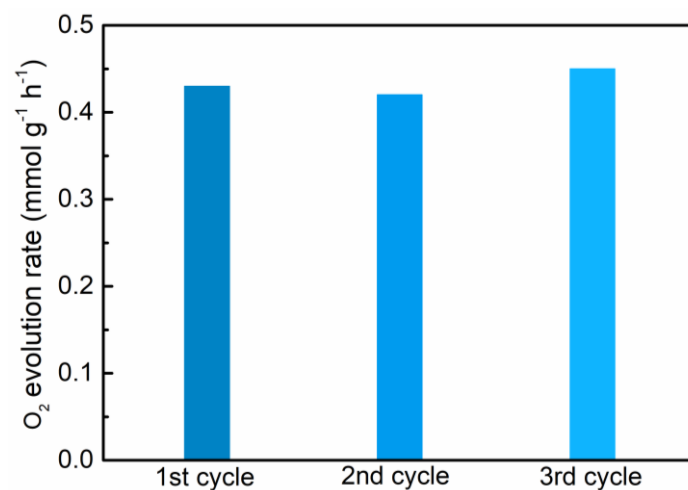


**Figure S14.** Cycling test of O<sub>2</sub> evolution over YF<sub>3</sub>: Yb, Tm@BiOCl under the irradiation of near-infrared light.

Figure S14 demonstrates the cycling test of the O<sub>2</sub> evolution process over YF<sub>3</sub>: Yb, Tm@BiOCl under the irradiation of near-infrared light. It can be observed that the water splitting process over YF<sub>3</sub>: Yb, Tm@BiOCl is stable.

**Table 1.** Summary of the oxygen evolution from water splitting by photocatalysts.

No.	Materials	Water oxidation		Reference
		420 nm < $\lambda$ < 800 nm	$\lambda$ > 800 nm	
1	Sr <sub>0.9</sub> NbO <sub>3</sub>	0.025 mmol g <sup>-1</sup> h <sup>-1</sup>	—	5
2	In <sub>0.26</sub> Ga <sub>0.74</sub> N: Mg: 200 °C	0.4 mmol g <sup>-1</sup> h <sup>-1</sup>	—	6
3	3.0 wt% (Pt) RuO <sub>2</sub> -loaded g-C <sub>3</sub> N <sub>4</sub>	0.0083 mmol g <sup>-1</sup> h <sup>-1</sup>	—	7
4	Ag <sub>3</sub> PO <sub>4</sub>	1.272 mmol g <sup>-1</sup> h <sup>-1</sup>	—	8
5	SrTiO <sub>3</sub> :La,Rh/Au/BiVO <sub>4</sub> :Mo (573K) Ru loaded	0.05 mmol h <sup>-1</sup>	—	9
6	BCN	0.012 mmol g <sup>-1</sup> h <sup>-1</sup>	—	10
7	IrO <sub>2</sub> -ZnDPEG (r=109)	0.015 mmol h <sup>-1</sup>	—	11
8	Pt(P.D.)/MnO <sub>x</sub> (P.D.)BiVO <sub>4</sub>	0.66 mmol g <sup>-1</sup> h <sup>-1</sup>	—	12
9	Pt/TiO <sub>2</sub> /Au	0.33 $\mu$ mol h <sup>-1</sup>	—	13
10	Carbon nanodot-C <sub>3</sub> N <sub>4</sub>	4.1 $\mu$ mol h <sup>-1</sup>	—	14
11	Ag-(001)BiOCl(110)-Pd	0.007 mmol g <sup>-1</sup> h <sup>-1</sup>	—	15
12	BiOCl with rich oxygen vacancies	0.36 mmol g <sup>-1</sup> h <sup>-1</sup>	—	16
13	YF <sub>3</sub> : Yb, Tm@BiOCl	0.49 mmol g <sup>-1</sup> h <sup>-1</sup>	0.43 mmol g <sup>-1</sup> h <sup>-1</sup>	This work

Table S1 indicates that the constructed epitaxial YF<sub>3</sub>: Yb, Tm@BiOCl presents outstanding water oxidation properties. The NIR-driven oxygen evolution rate of YF<sub>3</sub>: Yb, Tm@BiOCl is comparable to or even higher than those of BiOCl or some other catalytic systems under illumination by visible light. By comparing the electrons consumed by the oxygen evolution process and the incident photons, the quantum yield of oxygen evolution under the NIR light is estimated to be about 1.1%. More importantly, the amount of the oxygen evolution in 4 h under the visible light is about 1.97 mmol/g. Thus, the amount of O atom in the oxygen is larger than the amount of oxygen stoichiometric in 1 g BiOCl. As a result, the oxygen evolution is derived from water splitting instead of BiOCl decomposition.

## References

- 1 J. Jiang, K. Zhao, X. Xiao, L. Zhang, *J. Am. Chem. Soc.* **2012**, *134*, 4473.
- 2 F. Wang, R. Deng, J. Wang, Q. Wang, Y. Han, H. Zhu, X. Chen, X. Liu, **2011**, *10*, 968-973 (2011).
- 3 A. V. Kir'yanov. in *Radiation Effects in Materials* (ed. Waldemar A. Monteiro) Ch. 01 (InTech, 2016).
- 4 M. Guan, C. Xiao, J. Zhang, S. Fan, R. An, Q. Cheng, J. Xie, M. Zhou, B. Ye, Y. Xie, *J. Am. Chem. Soc.* **2013**, *135*, 10411.
- 5 X. Xu, C. Randorn, P. Efstathiou, J. T. S. Irvine, **2012**, *11*, 595.
- 6 M. G. Kibria, F. A. Chowdhury, S. Zhao, B. AlOtaibi, M. L. Trudeau, H. Guo, Z. Mi, *Nat. Commun.* **2015**, *6*, 6797.
- 7 X. Wang, K. Maeda, A. Thomas, K. Takanabe, G. Xin, J. M. Carlsson, K. Domen, M. Antonietti, *Nature Mater.* **2009**, *8*, 76.
- 8 Z. Yi, J. Ye, N. Kikugawa, T. Kako, S. Ouyang, H. Stuart-Williams, H. Yang, J. Cao, W. Luo, Z. Li, Y. Liu, R. L. Withers, *Nature Mater.* **2010**, *9*, 559.

- 9 Q. Wang, T. Hisatomi, Q. Jia, H. Tokudome, M. Zhong, C. Wang, Z. Pan, T. Takata, M. Nakabayashi, N. Shibata, Y. Li, I. D. Sharp, A. Kudo, T. Yamada, K. Domen, *Nature Mater.* **2016**, *15*, 611.
- 10 C. Huang, C. Chen, M. Zhang, L. Lin, X. Ye, S. Lin, M. Antonietti, X. Wang, *Nat. Commun.* **2015**, *6*, 7698.
- 11 Y. S. Nam, A. P. Magyar, D. Lee, J. W. Kim, D. S. Yun, H. Park, T. S. Pollom Jr, D. A. Weitz, A. M. Belcher, *Nature Nanotech.* **2010**, *5*, 340.
- 12 R. Li, F. Zhang, D. Wang, J. Yang, M. Li, J. Zhu, X. Zhou, H. Han, C. Li, *Nat. Commun.* **2013**, *4*, 1432.
- 13 S. Mubeen, J. Lee, N. Singh, S. Krämer, G. D. Stucky, M. Moskovits, *Nature Nanotech.* **2013**, *8*, 247.
- 14 J. Liu, Y. Liu, N. Liu, Y. Han, X. Zhang, H. Huang, Y. Lifshitz, S. T. Lee, J. Zhong, Z. Kang, *Science* **2015**, *347*, 970.
- 15 S. Bai, X. Li, Q. Kong, R. Long, C. Wang, J. Jiang, Y. Xiong, *Adv. Mater.* **2015**, *27*, 3444.
- 16 D. Cui, L. Wang, K. Xu, L. Ren, L. Wang, Y. Yu, Y. Du, W. Hao, *J. Mater. Chem. A* **2018**, *6*, 2193.